Non-Fourier heat transfer in a radial fin saturated with a shape-dependent Al_2O_3–Ag/water hybrid nanofluid

Weiping Wu[†] Chi-Wang Shu[*]

Abstract

This paper investigates the thermal behavior of a radial fin saturated with a shape-dependent Al_2O_3–Ag/water hybrid nanofluid. The governing equation is derived from Maxwell–Cattaneo–Vernotte (MCV) non-Fourier heat conduction coupled with convection, radiation, and surface mass-exchange losses. A local discontinuous Galerkin (LDG) method is employed to evaluate fin efficiency across varying nanoparticle volume fractions, shapes, and other governing parameters. The results indicate that adding hybrid nanoparticles enhances the time-averaged fin efficiency, which increases monotonically with volume fraction and reaches its highest value for the sphere–platelet combination. In contrast, the efficiency decreases as the radius ratio (the ratio of the fin radius to the cylindrical base radius) increases, but rises with increasing thermal lag parameter. Furthermore, the wave speed depends on the nanoparticle volume fraction and shape, the conductivity coefficient, and the thermal lag parameter, but remains independent of the radius ratio. Meanwhile, intensifying convection, radiation, or mass exchange lowers the fin temperature in the long-time regime. These findings provide practical guidance for the design of nanofluid-enhanced, non-Fourier radial fins.

Keywords: non-Fourier heat transfer, radial fin, hybrid nanofluid, local discontinuous Galerkin method

2010 Mathematics Subject Classification (MSC): 65M60, 35L20, 80A20

1 Introduction

Fins, or extended surfaces, are structures attached to a base surface to enhance heat transfer. By conducting heat away from the base and dissipating it to the surrounding fluid through convection, radiation, and other heat-loss mechanisms, fins improve the overall thermal performance of a system. This straightforward concept has given rise to a broad spectrum of applications [1]. In electronic devices, fins are incorporated into heat sinks to maintain components within safe operating temperatures [2]. In air-conditioning and refrigeration systems, fin-and-tube heat exchangers rely on fins to enlarge the heat transfer area between the refrigerant and the ambient air [3]. Fins also find use in automotive combustion-chamber and heat-sink cooling, high-speed air-breathing engines, and solar collectors [4, 5]. Owing to this extensive applicability, the thermal performance of fins has remained an active research topic for many decades.

Many researchers have studied longitudinal fins with different cross-sectional shapes. The rectangular profile serves as a common baseline in fin studies. Kumar et al. [6] examined a longitudinal rectangular fin with temperature-varying thermal conductivity and derived the thermal profile using the DTM–Padé approximant. Ullah et al. [7] analyzed the thermal performance of a porous

[†]School of Mechanical Engineering, Nanjing Institute of Technology, Nanjing 211167, Jiangsu Province, P. R. China. E-mail: wuweiping40@njit.edu.cn.

[*]Corresponding author. Division of Applied Mathematics, Brown University, Providence, Rhode Island, 02912, USA. E-mail: chi-wang_shu@brown.edu.

triangular fin under simultaneous convection, radiation, and internal heat generation, accounting for fin motion. Riasat et al. [8] compared dovetail and rectangular fins with adiabatic tips wetted with a ZnO–SAE 50 nanolubricant using a collocation scheme, finding that heat transfer increases with surface emissivity. Trapezoidal and concave-parabolic profiles offer better volume-adjusted heat transfer performance with less material, making them well suited to weight-sensitive applications [9]. Hosseinzadeh et al. [10] investigated moving porous fins with trapezoidal, concave-parabolic, and convex-parabolic cross-sections and reported that the concave-parabolic profile achieved the highest efficiency among the three. Exponential [11, 12] and semi-spherical [13] profiles have similarly been explored to improve fin performance. Fin shape thus affects both the temperature distribution and heat transfer rate, though these studies are limited to longitudinal fins attached to a flat base surface.

Besides longitudinal fins, radial fins are also common in practice, notably on cylindrical surfaces such as rotating shafts [14]. Owing to their broad practical relevance, heat transfer in radial fins has been examined extensively using a variety of analytical and numerical approaches. Exact and semi-analytical treatments have addressed radial fins with property variations that depend on temperature or position. Moitsheki [15] obtained exact solutions for rectangular and hyperbolic radial fin profiles, assuming that both the thermal conductivity and the convective coefficient follow a power-law temperature dependence. A different form of nonuniformity was considered by Aziz and Rahman [16], who prescribed the conductivity of a functionally graded fin as a power-law function of the radial coordinate. Complementary numerical treatments have since targeted more complex physical effects. Jooma and Harley [17] modeled a porous radial fin, using a differential-transform semi-analytical solution as a benchmark for the accuracy of a Crank–Nicolson finite difference scheme. Patel and Meher [18] instead adopted a fractional-order energy balance for a convective radial fin, capturing the combined effects of internal heat generation and temperature-dependent conductivity. More recently, Waseem et al. [19] proposed a neuro-symbolic modeling framework, combining a physics-informed neural network with symbolic regression, to obtain both accurate numerical solutions and compact closed-form expressions for the temperature distribution and efficiency of a moving radial fin with radiative-convective losses, temperature-dependent conductivity, and internal heat absorption. These works are based on the classical Fourier law of heat conduction, which assumes an infinite speed of heat propagation. This assumption works well under normal steady conditions.

However, Fourier's law loses validity once the time scale of a thermal disturbance becomes comparable to the material's intrinsic relaxation time; in this regime, referred to as non-Fourier heat conduction, heat propagates as a wave of finite speed rather than diffusing instantaneously [20]. The Maxwell–Cattaneo–Vernotte (MCV) model [21–23] is the most widely used formulation of this effect, introducing a relaxation-time term into Fourier's law to enforce a finite propagation speed. Non-Fourier heat conduction in longitudinal fins has been studied extensively. Lin [24] presented an early analysis of this problem for a convective fin, finding that the non-Fourier deviation persists into the periodic steady state and intensifies as the base-temperature oscillation frequency rises. Ahmadikia et al. [25] derived analytical solutions for a straight fin subjected to periodic base temperature and heat flux, demonstrating the formation of thermal shock waves. More recently, Singh et al. [26] obtained closed-form temperature distributions for longitudinal fins with internal heat generation and periodic boundary conditions under both Fourier and non-Fourier frameworks. Ma et al. [27] applied the element differential method to non-Fourier heat conduction in a convective-radiative fin, showing pronounced transient deviations from Fourier solutions at larger relaxation times, despite only modest differences in time-averaged efficiency. Compared with longitudinal fins, the non-Fourier behavior of radial fins has received comparatively less attention, which the present work aims to address.

Another way to improve fin heat transfer is to change the working fluid. A nanofluid is typically prepared by dispersing small solid nanoparticles into a base fluid such as water or ethylene glycol [28]. Compared with the base fluid, a nanofluid usually has higher thermal conductivity [29]. Because of this property, nanofluids have been used to enhance heat transfer capability of the system [30, 31]. Sowmya et al. [32] studied the effect of different nanoparticle shapes in a molybdenum disulfide nanofluid flowing over a radial fin. Ouada et al. [33] analyzed the heat transfer characteristics of a moving longitudinal porous fin wetted with a ternary hybrid nanofluid using the Adomian decomposition method. Upadhyay et al. [34] used the Legendre wavelet collocation method to numerically study heat transfer in stretching and shrinking longitudinal fins with an exponential profile, including its tapered and retracted variants, cooled by a nanofluid. Pavithra and Gireesha [35] examined an exponential longitudinal fin immersed in a shape-dependent hybrid nanofluid, comparing Fourier and non-Fourier heat conduction models. In addition, Pavithra et al. [36] investigated a moving dovetail longitudinal fin cooled by a flowing hybrid nanofluid using the Hermite wavelet method. Taken together, these studies indicate that adding nanoparticles to the working fluid can further enhance the thermal performance of a fin, which motivates combining nanofluid cooling with radial fin geometries in the present work.

Motivated by these two gaps, the present work develops a unified model for the transient, non-Fourier heat transfer of a wet, porous radial fin saturated with a shape-dependent Al_2O_3–Ag hybrid nanofluid, incorporating combined convection, radiation, and mass-exchange surface losses. The resulting governing equation is a strongly nonlinear and closed-form solutions are generally unavailable, it is therefore solved numerically by a local discontinuous Galerkin (LDG) method [37] equipped with a TVB slope limiter [38] and a semi-implicit time-marching scheme. The method is shown to accurately capture the location and sharpness of the moving thermal wavefront without spurious oscillations, even for large values of the convection parameter. The validated scheme is then employed to systematically examine how the fin geometry, the thermal lag parameter, and the nanoparticle volume fraction and shape jointly govern the fin's transient response, wavefront propagation speed, and long-time efficiency.

The main contributions of this work are summarized as follows. First, we develop a transient, non-Fourier model for a radial fin, whereas most existing studies on radial fins are restricted to the steady state or to classical Fourier conduction; by introducing the radius ratio κ, the present formulation also avoids the singularity at $r = 0$ inherent in the model of Waseem et al. [19]. Second, unlike previous studies that compare nanoparticles of different materials assigned to different shapes, we fix the nanoparticle materials and vary only their shape combination, which more faithfully isolates the pure effect of particle shape on the fin efficiency. Third, we analyze how the governing parameters affect the wavefront propagation speed, showing that it is influenced by the nanoparticle volume fraction and shape, the conductivity coefficient, and the thermal lag parameter. Finally, our results reveal that increasing the fin's radial length does not necessarily improve its heat transfer efficiency, whereas appropriately adding an Al_2O_3–Ag hybrid nanofluid with the sphere–platelet combination yields a substantial efficiency gain, offering practical guidance for fin design in engineering applications.

2 Mathematical Formulation

We consider a thin, wet, porous radial fin mounted on a cylindrical base, saturated with a shape-dependent Al_2O_3–Ag/water hybrid nanofluid. As shown in Figure 1, the radius of the base is R_b, and the radial length of the fin is L. In this paper, we define $\kappa = L/R_b$ as the radius ratio of the fin. Heat transfer from the fin surface involves the combined mechanisms of convection, radiation, and mass exchange. The heat conduction within the fin is governed by the non-Fourier MCV constitutive law, which incorporates a finite thermal relaxation time and thereby captures the finite speed of thermal wave propagation.

2.1 Hybrid nanofluid properties

For $i = 1, 2$, let ϕ_i, ρ_i, c_i, k_{si} be the volume fraction, density, specific heat, and thermal conductivity of the i-th nanoparticle in the hybrid nanofluid, and let $\phi = \phi_1 + \phi_2$. The variables with subscript f mean the quantities of base fluid. The effective density of the hybrid nanofluid and the effective

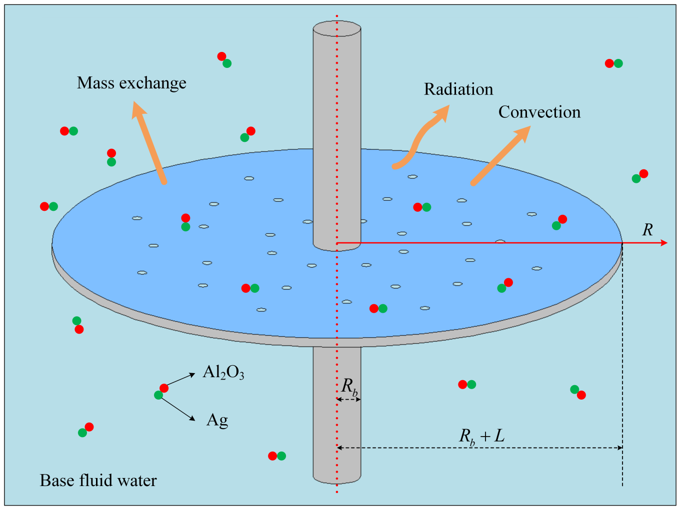

Figure 1: The coordinate system and configuration of a radial fin saturated with Al_2O_3–Ag/water hybrid nanofluid.

volumetric heat capacity are determined by [36, 39]

$$\rho_{hnf} = \rho_1\phi_1 + \rho_2\phi_2 + (1 - \phi_1 - \phi_2)\rho_f, \tag{1}$$

$$(\rho c)_{hnf} = \phi_1(\rho c)_1 + \phi_2(\rho c)_2 + (1 - \phi_1 - \phi_2)(\rho c)_f. \tag{2}$$

Furthermore, the effective specific heat is defined as

$$c_{hnf} \doteq \frac{(\rho c)_{hnf}}{\rho_{hnf}}. \tag{3}$$

Let s_i be the shape factor of the i-th nanoparticle, the hybrid nanofluid conductivity k_{hnf} is defined by the following procedure [36, 39]

$$\frac{k_{nf1}}{k_f} = \frac{k_{s1} + (s_1 - 1)k_f + (s_1 - 1)\phi_1(k_{s1} - k_f)}{k_{s1} + (s_1 - 1)k_f - \phi_1(k_{s1} - k_f)}, \tag{4}$$

$$\frac{k_{nf2}}{k_f} = \frac{k_{s2} + (s_2 - 1)k_f + (s_2 - 1)\phi_2(k_{s2} - k_f)}{k_{s2} + (s_2 - 1)k_f - \phi_2(k_{s2} - k_f)}, \tag{5}$$

$$k_{hnf} = \frac{\phi_1 k_{nf1} + \phi_2 k_{nf2}}{\phi}. \tag{6}$$

Following [40], the shape factor $s = 3$ for spherical nanoparticles, $s = 4.9$ for cylindrical nanoparticles, and $s = 5.7$ for platelet-shaped nanoparticles.

2.2 Governing equation

The following assumptions are invoked in formulating the model: (i) the fin is axisymmetric, so that the temperature is independent of the azimuthal angle; (ii) the fin is geometrically slender, i.e., the fin thickness is uniform and much smaller than its radial length, so that the cross-sectional area and perimeter vary slowly with R; and (iii) the fin material is thermally isotropic, so that a single effective conductivity governs conduction in both the radial and through-thickness directions. Assumptions (i) and (ii) imply that the temperature varies only with the radial coordinate R and time t, so that the governing equation reduces to one spatial dimension.

The governing equation is derived from the energy balance equation

$$(\rho c)_{hnf}\,\frac{\partial T}{\partial t}+\frac{1}{R}\frac{\partial}{\partial R}\big(R\,q\big)=-\Phi(T) \tag{7}$$

together with the MCV constitutive relation

$$\tau_q\frac{\partial q}{\partial t}+q=-K_{hnf}(T)\,\frac{\partial T}{\partial R}, \tag{8}$$

where $\Phi(T)$ contains three surface-loss terms: convection, radiation, and mass exchange, namely

$$\Phi(T)=\frac{2}{\delta_b}\Big[h_a\Big(\frac{T-T_a}{T_b-T_a}\Big)^{\ell}(T-T_a)+\sigma\varepsilon^{*}F_{f-a}\big(T^4-T_a^4\big)+\dot{m}\,c_{hnf}(T-T_a)\Big], \tag{9}$$

and $K_{hnf}(T)$ is a temperature-dependent thermal conductivity given as [19, 35, 41]

$$K_{hnf}(T)=k_{hnf}\left[1+\delta\,(T-T_a)\right]. \tag{10}$$

In the above equations, $T=T(R,t)$ is the temperature, $R\in[R_b,\,R_b+L]$ is the radial coordinate, t is time, q is the heat flux, δ_b is fin thickness, and T_a is the temperature of the surrounding fluid. The parameter τ_q is the thermal relaxation time and δ is the temperature coefficient of thermal conductivity, while σ and ε^* denote the Stefan–Boltzmann constant and the effective surface emissivity, respectively, and F_{f-a} is the radiation view factor between the fin surface and the ambient. The quantity $\dot{m}$ is the mass flux of moisture evaporating from the wet, porous fin surface into the ambient. The coefficient h_a is the convective heat-transfer coefficient at the fin surface, taken as a constant representative of the ambient convective environment. The exponent ℓ depends on the prevailing heat-transfer mode: for example, $\ell=1/4$ corresponds to laminar natural convection and $\ell=1/3$ to turbulent natural convection [42, 43].

To derive the governing equation, we differentiate (7) with respect to t,

$$(\rho c)_{hnf}\frac{\partial^2 T}{\partial t^2}+\frac{1}{R}\frac{\partial}{\partial R}\Big(R\frac{\partial q}{\partial t}\Big)=-\frac{\partial\Phi}{\partial t}. \tag{11}$$

Substituting (8) into the above equation and multiplying by τ_q yields

$$(\rho c)_{hnf}\tau_q\frac{\partial^2 T}{\partial t^2}-\frac{1}{R}\frac{\partial}{\partial R}(Rq)-\frac{1}{R}\frac{\partial}{\partial R}\Big(RK_{hnf}(T)\frac{\partial T}{\partial R}\Big)=-\tau_q\frac{\partial\Phi}{\partial t}. \tag{12}$$

Adding (7) and (12) and neglecting the high-order term $-\tau_q\frac{\partial\Phi}{\partial t}$ leads to the governing equation

$$(\rho c)_{hnf}\Big(\tau_q\frac{\partial^2 T}{\partial t^2}+\frac{\partial T}{\partial t}\Big)=\frac{1}{R}\frac{\partial}{\partial R}\Big(R\,K_{hnf}(T)\frac{\partial T}{\partial R}\Big)-\Phi(T). \tag{13}$$

The initial condition is [35, 39]

$$T(R,0)=T_a,\qquad \left.\frac{\partial T}{\partial t}\right|_{t=0}=0. \tag{14}$$

Assume the fin tip is insulated and the temperature at the fin base is T_b, namely [19, 39]

$$T(R_b,t)=T_b,\qquad \left.\frac{\partial T}{\partial R}\right|_{R=R_b+L}=0. \tag{15}$$

2.3 Dimensionless governing equation

Introducing the following non-dimensionalization variables

$$
\begin{aligned}
&r = \frac{R - R_b}{L}, \quad \tau = \frac{k_f}{(\rho c)_f L^2} t, \quad \theta = \frac{T}{T_b}, \quad \theta_a = \frac{T_a}{T_b}, \quad V_e = \sqrt{\frac{k_f \tau_q}{(\rho c)_f L^2}}, \\
&\delta^* = \delta T_b, \quad M^2 = \frac{2\, h_a\, L^2}{k_f\, \delta_b}, \quad R_n = \frac{2\sigma\varepsilon^* F_{f-a} T_b^3 L^2}{k_f\, \delta_b}, \quad S_m = \frac{2\, \dot{m}\, c_f\, L^2}{k_f\, \delta_b},
\end{aligned}
\tag{16}
$$

and defining

$$
\Lambda_k = \frac{k_{hnf}}{k_f}, \quad \Lambda_\rho = \frac{\rho_{hnf}}{\rho_f}, \quad \Lambda_c = \frac{c_{hnf}}{c_f}, \quad \Lambda_{\rho c} = \frac{(\rho c)_{hnf}}{(\rho c)_f}, \quad \Lambda_D = \frac{\Lambda_k}{\Lambda_{\rho c}},
\tag{17}
$$

the governing equation can be reduced into the dimensionless form

$$
\begin{aligned}
V_e^2 \frac{\partial^2 \theta}{\partial \tau^2} + \frac{\partial \theta}{\partial \tau} =& \Lambda_D \, \frac{1}{1+\kappa r} \frac{\partial}{\partial r} \Big[(1+\kappa r)\big(1 + \delta^*(\theta - \theta_a)\big) \frac{\partial \theta}{\partial r} \Big] \\
&- \Big[M^2 \Lambda_{\rho c}^{-1} \frac{(\theta - \theta_a)^{\ell+1}}{(1-\theta_a)^{\ell}} + R_n \Lambda_{\rho c}^{-1} (\theta^4 - \theta_a^4) + S_m \Lambda_\rho^{-1} (\theta - \theta_a) \Big],
\end{aligned}
\tag{18}
$$

for $0 \le r \le 1$.

Correspondingly, the initial and boundary conditions turn out

$$
\text{Initial condition:} \qquad \theta(r, 0) = \theta_a, \qquad \left.\frac{\partial \theta}{\partial \tau}\right|_{\tau=0} = 0.
\tag{19}
$$

$$
\text{Boundary condition:} \qquad \theta(0, \tau) = 1, \qquad \left.\frac{\partial \theta}{\partial r}\right|_{r=1} = 0.
\tag{20}
$$

3 Numerical Methods

Defining $\tilde{\theta} = \theta - \theta_a$ and introducing two auxiliary variables $w = \partial\tilde{\theta}/\partial\tau$, $p = \partial\tilde{\theta}/\partial r$, the dimensionless governing equation is reformulated to a first-order system

$$
\begin{cases}
\dfrac{\partial \tilde{\theta}}{\partial \tau} = w, \\
p = \dfrac{\partial \tilde{\theta}}{\partial r}, \\
\dfrac{\partial w}{\partial \tau} = -\dfrac{1}{V_e^2} w + \dfrac{\Lambda_D}{V_e^2} \dfrac{1}{1+\kappa r} \dfrac{\partial}{\partial r} \big[(1+\kappa r)\big(1 + \delta^* \tilde{\theta}\big) p \big] - \dfrac{1}{V_e^2} g(\tilde{\theta}, r),
\end{cases}
\tag{21}
$$

where

$$
g(\tilde{\theta}, r) = M^2 \Lambda_{\rho c}^{-1} \frac{\tilde{\theta}^{\,\ell+1}}{(1-\theta_a)^{\ell}} + R_n \Lambda_{\rho c}^{-1} \big[(\tilde{\theta} + \theta_a)^4 - \theta_a^4 \big] + S_m \Lambda_\rho^{-1} \tilde{\theta}.
\tag{22}
$$

Expanding the divergence term in the last equation, we obtain

$$
\frac{\partial w}{\partial \tau} = -\frac{1}{V_e^2} w + \frac{\Lambda_D}{V_e^2} \Big(\frac{\partial p}{\partial r} + \delta^* \frac{\partial (\tilde{\theta} p)}{\partial r} \Big) + \frac{\Lambda_D}{V_e^2} \frac{\kappa}{1+\kappa r} \big(1 + \delta^* \tilde{\theta}\big) p - \frac{1}{V_e^2} g(\tilde{\theta}, r).
\tag{23}
$$

Building on this reformulation, we discretize $[0, 1]$ into J non-overlapping elements $I_j = (r_{j-\frac{1}{2}}, r_{j+\frac{1}{2}})$, $j = 1, \ldots, J$, with $r_{\frac{1}{2}} = 0$ and $r_{J+\frac{1}{2}} = 1$, and work in the piecewise polynomial space

$$
V_h = \{ u \in L^2([0, 1]) \colon u|_{I_j} \in \mathcal{P}^n(I_j),\ 1 \le j \le J \},
\tag{24}
$$

where $\mathcal{P}^n(I_j)$ collects polynomials of degree at most n ($n \geq 0$) on I_j. Because elements of V_h are generally discontinuous at the mesh interfaces, for $u \in V_h$ we write $u^+_{j+\frac{1}{2}}$ and $u^-_{j+\frac{1}{2}}$ for its right- and left-hand traces at $r_{j+\frac{1}{2}}$,

$$u^+_{j+\frac{1}{2}} = \lim_{\varepsilon \to 0^+} u(r_{j+\frac{1}{2}} + \varepsilon), \quad u^-_{j+\frac{1}{2}} = \lim_{\varepsilon \to 0^+} u(r_{j+\frac{1}{2}} - \varepsilon). \tag{25}$$

The LDG discretization of (21) is then obtained by testing each equation against $v_h \in V_h$ and integrating by parts on every element: find $\tilde{\theta}_h, p_h, w_h \in V_h$ such that, for all $v_h \in V_h$ and every I_j,

$$\begin{aligned}
\int_{I_j} \frac{\partial \tilde{\theta}_h}{\partial \tau} v_h \, dr &= \int_{I_j} w_h v_h \, dr, \\
\int_{I_j} p_h v_h \, dr &= -\int_{I_j} \tilde{\theta}_h \frac{\partial v_h}{\partial r} \, dr + \widehat{\tilde{\theta}}_{h_{j+\frac{1}{2}}} v^-_{h_{j+\frac{1}{2}}} - \widehat{\tilde{\theta}}_{h_{j-\frac{1}{2}}} v^+_{h_{j-\frac{1}{2}}}, \\
\int_{I_j} \frac{\partial w_h}{\partial \tau} v_h \, dr &= -\frac{1}{V_e^2} \int_{I_j} w_h v_h \, dr + \frac{\Lambda_D}{V_e^2} \left[-\int_{I_j} p_h \frac{\partial v_h}{\partial r} \, dr + \widehat{p_h}_{j+\frac{1}{2}} v^-_{h_{j+\frac{1}{2}}} - \widehat{p_h}_{j-\frac{1}{2}} v^+_{h_{j-\frac{1}{2}}} \right] \\
&\quad + \frac{\Lambda_D \delta^*}{V_e^2} \left[-\int_{I_j} \tilde{\theta}_h p_h \frac{\partial v_h}{\partial r} \, dr + \widehat{\tilde{\theta}_h p_h}_{j+\frac{1}{2}} v^-_{h_{j+\frac{1}{2}}} - \widehat{\tilde{\theta}_h p_h}_{j-\frac{1}{2}} v^+_{h_{j-\frac{1}{2}}} \right] \\
&\quad + \int_{I_j} \left[\frac{\Lambda_D}{V_e^2} \frac{\kappa}{1 + \kappa r} (1 + \delta^* \tilde{\theta}_h) p_h - \frac{1}{V_e^2} g(\tilde{\theta}_h, r) \right] v_h \, dr.
\end{aligned} \tag{26}$$

Well-posedness of this element-wise formulation hinges on a consistent choice of the numerical fluxes, which are selected as

Interface	$\widehat{\tilde{\theta}}_h$	$\widehat{p_h}$	$\widehat{\tilde{\theta}_h p_h}$
$j = 0$	$1 - \theta_a$	$p_h{}^+_{\frac{1}{2}}$	$(\tilde{\theta}_h p_h)^+_{\frac{1}{2}}$
$j = 1, \dots, J-1$	$(\tilde{\theta}_h)^-_{j+\frac{1}{2}}$	$p_h{}^+_{j+\frac{1}{2}}$	$(\tilde{\theta}_h p_h)^+_{j+\frac{1}{2}}$
$j = J$	$(\tilde{\theta}_h)^-_{J+\frac{1}{2}}$	0	0

where the $j = 0$ and $j = J$ cases enforce the prescribed boundary value $\theta = 1$ at $r = 0$ and a homogeneous Neumann flux at $r = 1$, respectively, while the interior interfaces adopt an alternating flux pair [44].

To turn this variational statement into an algebraic system, each unknown is represented locally by

$$u(r, \tau) = \sum_{i=0}^{n} u^i_j(\tau) \, \psi^i_j(r), \quad \forall \, r \in I_j, \tag{27}$$

with $\{\psi^i_j\}_{i=0}^n$ a basis of $\mathcal{P}^n(I_j)$ and $\{u^i_j(\tau)\}_{i=0}^n$ the associated degrees of freedom. Inserting these expansions for $\tilde{\theta}_h, p_h, w_h$ into the scheme above and taking $v_h = \psi^\ell_j(r)$, $\ell = 0, \dots, n$, on every element converts the weak formulation into a semi-discrete system of ODEs,

$$\begin{cases}
\dot{\tilde{\boldsymbol{\theta}}}_h = \boldsymbol{w}_h, \\
\boldsymbol{p}_h = \boldsymbol{A}^-_h(\tilde{\boldsymbol{\theta}}_h), \\
\mathbb{M} \, \dot{\boldsymbol{w}}_h = -\dfrac{1}{V_e^2} \, \boldsymbol{w}_h + \dfrac{\Lambda_D}{V_e^2} \, \boldsymbol{A}^+_h(\boldsymbol{p}_h) + \dfrac{\Lambda_D \delta^*}{V_e^2} \, \boldsymbol{A}^+_h(\tilde{\boldsymbol{\theta}}_h \boldsymbol{p}_h) + \boldsymbol{S}_h(\boldsymbol{p}_h, \tilde{\boldsymbol{\theta}}_h),
\end{cases} \tag{28}$$

where $\tilde{\boldsymbol{\theta}}_{\boldsymbol{h}}, \boldsymbol{p}_{\boldsymbol{h}}, \boldsymbol{w}_{\boldsymbol{h}}$ denote the vectors of degrees of freedom of $\tilde{\theta}_h, p_h, w_h$, $\mathbb{M}$ is the mass matrix, the operators $\boldsymbol{A}^-_h$ and $\boldsymbol{A}^+_h$ realize the LDG discretization under the two flux conventions used above, and $\boldsymbol{S}_{\boldsymbol{h}}$ absorbs all remaining source contributions.

Next, the above semi-discrete system is advanced in time by the following algorithm. Starting from the initial data $\theta_h^0 = P_h\theta(0)$ and $w_h^0 = P_h\theta_t(0)$, obtained by taking the local L^2 projection of the initial condition, we set $\tilde{\theta}_h^0 = \theta_h^0 - \theta_a$ and apply the TVB limiter [38] to obtain $\tilde{\theta}_{h,*}^0$. Given $(\tilde{\boldsymbol{\theta}}_{h,*}^m, \boldsymbol{w}_h^m)$ at time level m, the numerical solution is advanced to time level $m+1$ through the following four steps:

$$
\begin{aligned}
&\text{Step 1:} \quad \tilde{\boldsymbol{\theta}}_h^{m+1} = \tilde{\boldsymbol{\theta}}_{h,*}^m + \Delta\tau\, \boldsymbol{w}_h^m \\
&\text{Step 2:} \quad \boldsymbol{p}_h^{m+1} = \boldsymbol{A}_h^-(\tilde{\boldsymbol{\theta}}_h^{m+1}) \\
&\text{Step 3:} \quad \tilde{\boldsymbol{\theta}}_h^{m+1} \xrightarrow{\text{TVB limiter}} \tilde{\boldsymbol{\theta}}_{h,*}^{m+1} \\
&\text{Step 4:} \quad \mathbb{M}\, \boldsymbol{w}_h^{m+1} = \mathbb{M}\, \boldsymbol{w}_h^m - \frac{\Delta\tau}{V_e^2}\boldsymbol{w}_h^m + \Delta\tau\, \boldsymbol{H}(\boldsymbol{p}_h^{m+1}, \tilde{\boldsymbol{\theta}}_{h,*}^{m+1})
\end{aligned}
\tag{29}
$$

where $\Delta\tau$ is the time step and

$$
\boldsymbol{H}(\boldsymbol{p}_h, \tilde{\boldsymbol{\theta}}_h) := \frac{\Lambda_D}{V_e^2}\, \boldsymbol{A}_h^+(\boldsymbol{p}_h) + \frac{\Lambda_D \delta^*}{V_e^2}\, \boldsymbol{A}_h^+(\tilde{\boldsymbol{\theta}}_h \boldsymbol{p}_h) + \boldsymbol{S}_h(\boldsymbol{p}_h, \tilde{\boldsymbol{\theta}}_h). \tag{30}
$$

This procedure is repeated for $m = 0, 1, \ldots, M-1$, and the temperature approximation at the final time is recovered from $\theta_h^M = \tilde{\theta}_h^M + \theta_a$.

4 Results and Discussion

4.1 Verification

Taking $V_e = \Lambda_D = \Lambda_{\rho c}^{-1} = 1$, $\delta^* = \ell = R_n = S_m = 0$ in (18), the following initial-boundary value problem

$$
\begin{cases}
\frac{\partial^2\theta}{\partial\tau^2} + \frac{\partial\theta}{\partial\tau} = \frac{\partial^2\theta}{\partial r^2} - M^2(\theta - \theta_a), \\
\theta(r, 0) = \theta_a, \quad \frac{\partial\theta}{\partial\tau}(r, 0) = 0, \\
\theta(0, \tau) = 1, \quad \frac{\partial\theta}{\partial r}(1, \tau) = 0,
\end{cases}
\tag{31}
$$

is used to verify the algorithm proposed in the previous section. The analytical solution of (31) can be obtained by separation of variables, which is (see the detailed deduction in Appendix A)

$$
\theta(r, \tau) = \theta_a + (1 - \theta_a)\frac{\cosh[M(1-r)]}{\cosh M} + e^{-\tau/2}\sum_{n=1}^{\infty}\left[a_n\cos(\mu_n\tau) + \frac{a_n}{2\mu_n}\sin(\mu_n\tau)\right]\sin(\lambda_n r), \tag{32}
$$

where

$$
\lambda_n = \frac{(2n-1)\pi}{2}, \qquad \mu_n = \sqrt{M^2 + \lambda_n^2 - \frac{1}{4}}, \qquad a_n = -\frac{2(1-\theta_a)\lambda_n}{M^2 + \lambda_n^2}. \tag{33}
$$

Figure 2 compares the numerical solutions obtained with $J = 1000$ and $J = 2000$ mesh elements against the analytical solution (32) — with the infinite series truncated at 10000 terms — at $\tau = 0.5$, for three representative values of the parameter M: $M = 1$, 10, and 100. It can be observed that the numerical solutions computed on the two meshes are in close agreement over the entire domain for $M = 1$ and $M = 10$, and remain in good agreement for $M = 100$ with only minor differences before the wave front, which indicates that the scheme converges as the mesh is refined. Moreover, compared with the analytical solutions shown in the right column, one can see that the numerical scheme accurately captures both the location and the strength of the discontinuity at $r = 0.5$; as the mesh is refined from $J = 1000$ to $J = 2000$, the numerical transition across the front becomes visibly sharper. Notably, unlike the truncated-series analytical solution, which exhibits pronounced Gibbs oscillations in the neighborhood of the discontinuity (most evident for $M = 100$), the numerical solution is essentially free of spurious oscillations at the front for all three values of M, demonstrating the effectiveness of our method in suppressing overshoots while still resolving the discontinuity sharply. This behavior is consistent across the wide range of M considered, indicating that the robustness of the scheme is not sensitive to the strength of the convection term.

Figure 2 reports the corresponding comparison at $\tau = 20$ when the system approaches steady state. The excellent agreement between the numerical and analytical solutions observed for all three values of M confirms the correctness of the numerical scheme in long-time simulations.

4.2 Comparison of fin efficiency between different volume fractions ϕ and nanoparticles with different shape

To isolate the pure effect of nanoparticle shape, we avoid the confounding approach in [35, 36, 39], where different shapes were compared using different materials. Here, the first nanoparticle is fixed as spherical Al_2O_3 ($s_1 = 3$) and the second nanoparticle as Ag, with the latter's shape factor swept across sphere ($s_2 = 3$, "SS"), cylinder ($s_2 = 4.9$, "SC"), and platelet ($s_2 = 5.7$, "SP"), all in a water base fluid. The thermophysical properties are given in Table 1.

Table 1: Thermophysical properties [39].

	Water	Al_2O_3	Ag
$\rho\,(\mathrm{kg\,m^{-3}})$	997.1	3970	10500
$c_p\,(\mathrm{J\,kg^{-1}K^{-1}})$	4179	765	235
$k\,(\mathrm{W\,m^{-1}K^{-1}})$	0.613	40	429

Based on these material properties, the density, volumetric heat capacity, and specific heat capacity of the resulting Al_2O_3–Ag/water hybrid nanofluid are evaluated at the three total volume fractions considered in this study, $\phi = 1\%, 2\%, 4\%$ (with $\phi_1 = \phi_2 = \phi/2$); the corresponding values are summarized in Table 2.

Table 2: Thermophysical properties of the hybrid nanofluid at different volume fractions ϕ.

ϕ	ρ_{hnf} $(\mathrm{kg\,m^{-3}})$	$(\rho c)_{hnf}$ $(\mathrm{J\,m^{-3}K^{-1}})$	c_{hnf} $(\mathrm{J\,kg^{-1}K^{-1}})$
1%	1059.48	4.1527×10^6	3919.60
2%	1121.86	4.1386×10^6	3689.05
4%	1246.62	4.1103×10^6	3297.16

Combining the properties in Tables 1 and 2 with the shape-dependent correlations for the effective thermal conductivity and thermal diffusivity yields the factors Λ_k, Λ_D, Λ_ρ^{-1}, and $\Lambda_{\rho c}^{-1}$ that appear in the governing system (21). These factors are reported in Table 3 for the base fluid ($\phi = 0$) and for each of the nine shape–concentration combinations, indexed 1–9 for reference in the figures that follow. As expected, Λ_ρ^{-1} and $\Lambda_{\rho c}^{-1}$ depend only on the volume fraction ϕ and are insensitive to the shape combination, whereas Λ_k and Λ_D increase with ϕ and, for fixed ϕ, consistently follow the order SP > SC > SS.

To quantify how these property variations translate into fin performance, we define the fin efficiency as the ratio of the actual heat transfer rate from the fin to that of an ideal fin whose entire surface is maintained at the base temperature. The actual and ideal heat transfer rates are given, respectively, by

$$Q_{fin} = \int_0^1 \Big[M^2 \Lambda_{\rho c}^{-1} \frac{(\theta - \theta_a)^{\ell+1}}{(1-\theta_a)^{\ell}} + R_n \Lambda_{\rho c}^{-1} (\theta^4 - \theta_a^4) + S_m \Lambda_\rho^{-1} (\theta - \theta_a) \Big] (1 + \kappa r)\, dr, \tag{34}$$

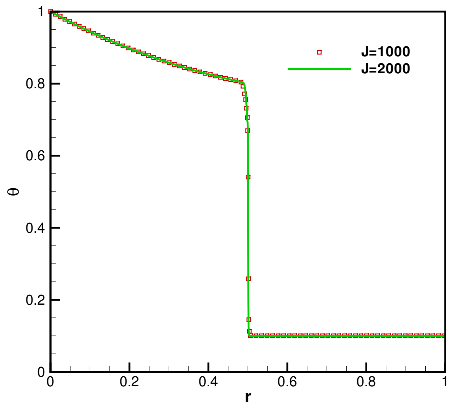

(a) $M = 1$, numerical

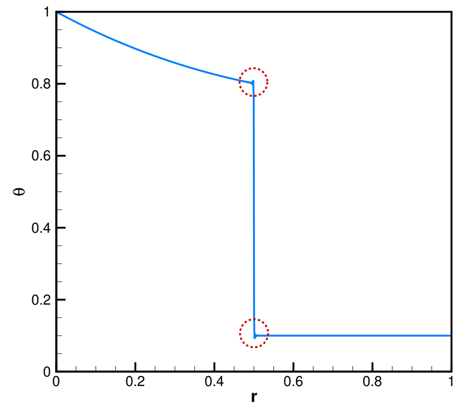

(b) $M = 1$, analytical

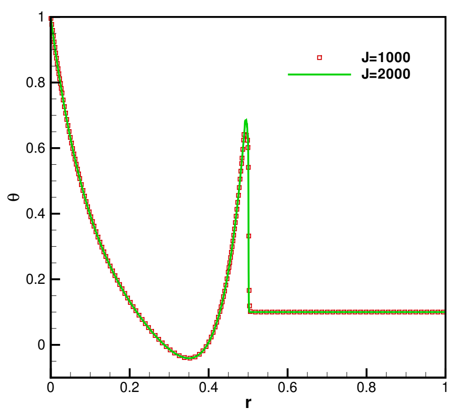

(c) $M = 10$, numerical

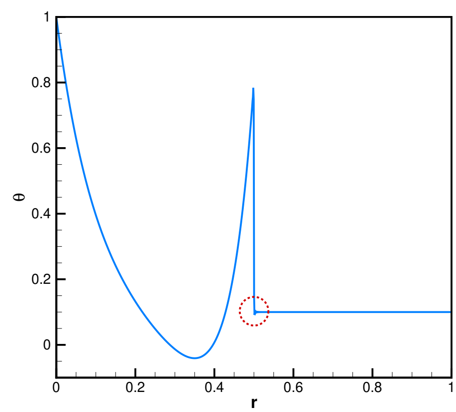

(d) $M = 10$, analytical

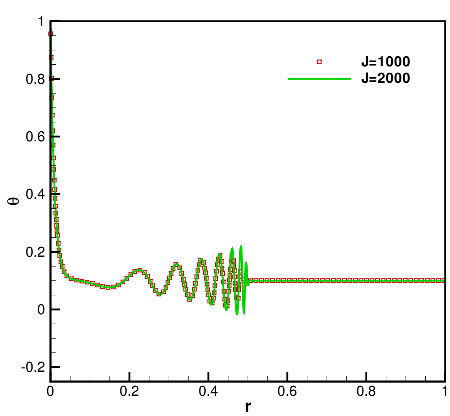

(e) $M = 100$, numerical

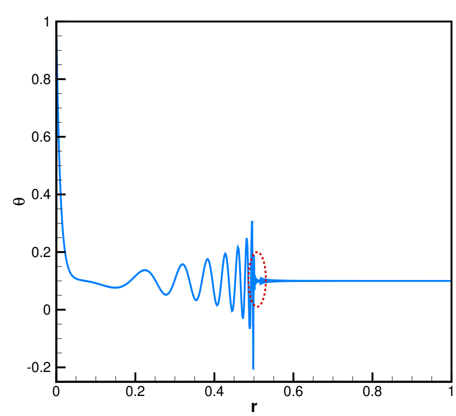

(f) $M = 100$, analytical

Figure 2: Comparison of the numerical solutions with mesh elements $J = 1000, 2000$ with the analytical solution of (31) at $\tau = 0.5$, for different value of M.

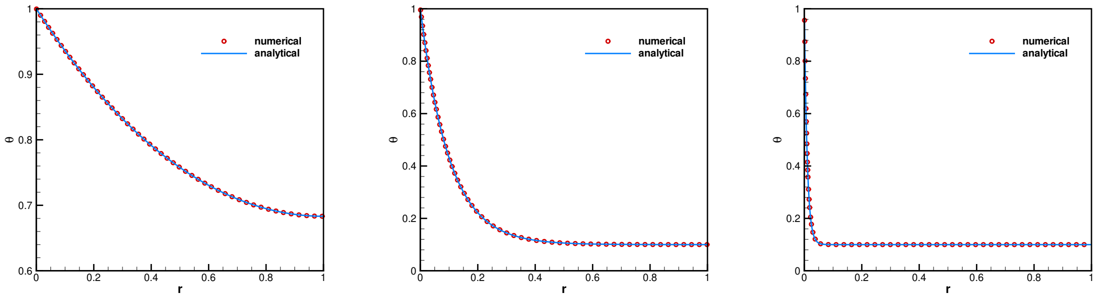

(a) $M = 1$ (b) $M = 10$ (c) $M = 100$

Figure 3: Comparison of the numerical solutions with mesh elements $J = 1000$ with the analytical solution of (31) at $\tau = 20$, for different value of M.

Table 3: The values of Λ_k, Λ_D, Λ_ρ^{-1} and $\Lambda_{\rho c}^{-1}$ for the Al_2O_3–Ag shape sweep, at three concentrations.

	$\phi = 0$	$\phi_1 = \phi_2 = 0.5\%$ ($\phi = 1\%$)			$\phi_1 = \phi_2 = 1\%$ ($\phi = 2\%$)			$\phi_1 = \phi_2 = 2\%$ ($\phi = 4\%$)		
	–	SS	SC	SP	SS	SC	SP	SS	SC	SP
index	0	1	2	3	4	5	6	7	8	9
Λ_k	1	1.0147	1.0194	1.0214	1.0296	1.0390	1.0430	1.0597	1.0789	1.0869
Λ_D	1	1.0182	1.0229	1.0249	1.0366	1.0462	1.0502	1.0743	1.0937	1.1019
Λ_ρ^{-1} [a]	1		0.9411			0.8888			0.7999	
$\Lambda_{\rho c}^{-1}$ [a]	1		1.0034			1.0068			1.0138	

[a] Independent of the nanoparticle shape combination (SS, SC, SP).

$$Q_{ideal} = \left(1 + \frac{\kappa}{2}\right)\left[M^2\Lambda_{\rho c}^{-1}(1-\theta_a) + R_n\Lambda_{\rho c}^{-1}(1-\theta_a^4) + S_m\Lambda_\rho^{-1}(1-\theta_a)\right], \tag{35}$$

so that the instantaneous fin efficiency reads

$$\textit{fin efficiency: } \eta = \frac{Q_{fin}}{Q_{ideal}}. \tag{36}$$

Since $\eta(\tau)$ evolves in time as the fin approaches its steady state, we further report the time-averaged efficiency over the interval $[0, \tau^*]$, defined by

$$\bar{\eta}(\tau^*) = \frac{1}{\tau^*}\int_0^{\tau^*} \eta(\tau)\, d\tau, \tag{37}$$

which is used in the remainder of this subsection to compare the performance of the base fluid ($\phi = 0$, index 0) against the nine shape–concentration combinations introduced above (indices 1–9).

As shown in Figure 4, under otherwise identical conditions, the addition of hybrid nanoparticles always increases the time-averaged efficiency $\bar{\eta}$ relative to the pure base fluid, and $\bar{\eta}$ increases monotonically as the case index increases from 1 to 9. For example, in Figure 4(a) for the case $\kappa = 1$, the efficiency at index 9 ($\phi = 4\%$, SP) is about 5.78% higher than at index 0 ($\phi = 0$), illustrating the substantial gains achievable with hybrid nanoparticles. Since the index steps the volume fraction ϕ up in three stages (indices 1–3, 4–6, 7–9; see Table 3), this confirms that the efficiency increases with ϕ. In addition, within each concentration group the ordering SP > SC > SS holds consistently, showing that the SP combination yields the highest efficiency among the three shape combinations. This ordering directly mirrors that of the factors Λ_k and Λ_D reported in Table 3: larger Λ_k and Λ_D

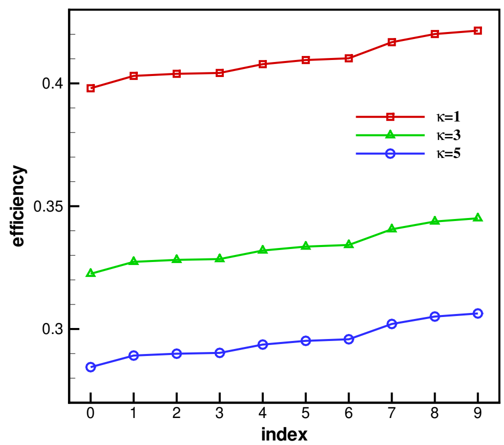

(a) effect of κ

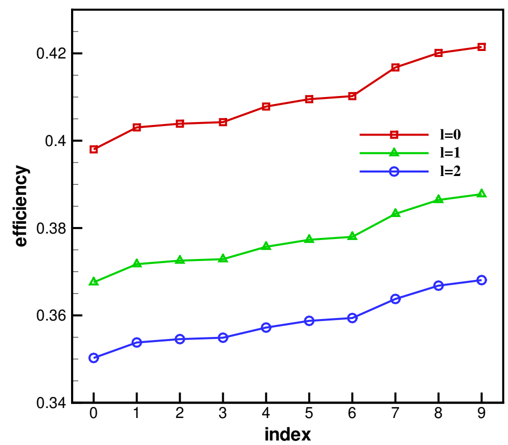

(b) effect of ℓ

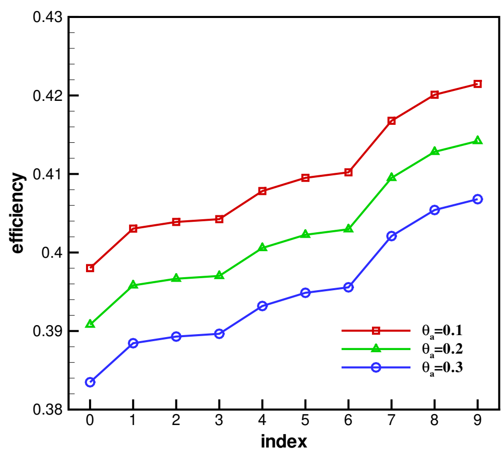

(c) effect of θ_a

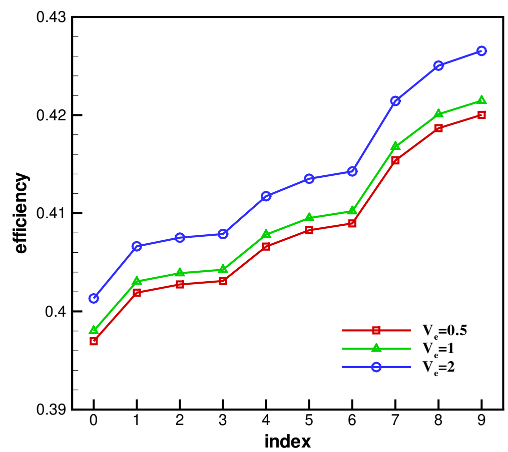

(d) effect of V_e

Figure 4: Comparison of the time-averaged efficiency $\bar{\eta}(\tau^* = 20)$ between the pure base fluid without hybrid nanoparticles (index 0) and the nine shape–concentration combinations (indices 1–9). Common parameters: $\delta^* = 0.1$, $M^2 = R_n = S_m = 1$. (a) effect of κ, other parameters: $\ell = 0$, $\theta_a = 0.1$, $V_e = 1$; (b) effect of ℓ, other parameters: $\kappa = 1$, $\theta_a = 0.1$, $V_e = 1$; (c) effect of θ_a, other parameters: $\kappa = 1$, $\ell = 0$, $V_e = 1$; (d) effect of V_e, other parameters: $\ell = 0$, $\kappa = 1$, $\theta_a = 0.1$.

indicate a stronger enhancement of the effective thermal conductivity and diffusivity of the hybrid nanofluid, which in turn improves heat conduction along the fin and increases its efficiency.

Figure 4(a) shows that the efficiency decreases as $\kappa = L/R_b$ increases. Since a larger κ corresponds to a longer fin relative to the radius of base, the heat has a longer distance to travel from the base to the tip. As a result, the temperature drops well below the base value over much of the fin, leaving little temperature difference to drive further heat loss there. This suggests that extending the fin length beyond a certain point yields little additional heat dissipation, so the added material is largely wasted. A more effective design strategy is therefore to choose a moderate κ rather than to pursue an overly long fin.

Figure 4(b) shows that the efficiency decreases as ℓ increases. The reason is that a larger ℓ concentrates the heat generation more strongly near the base, so only the region close to the base contributes significantly to heat dissipation. This implies that, when the underlying heat-loss mechanism is strongly nonlinear (e.g., turbulent convection), simply extending the fin does not help much, since most of its length no longer contributes effectively.

Figure 4(c) shows that the efficiency decreases as θ_a increases, meaning that fins are less efficient when operating in warmer surroundings. In such environments, the overall temperature difference driving heat transfer is smaller everywhere, which weakens the nonlinear enhancement effects from radiation and temperature-dependent conductivity that normally help spread heat along the fin, so the actual fin falls further short of the ideal case.

Figure 4(d) shows that the time-averaged efficiency over $[0, \tau^* = 20]$ increases as V_e increases. A larger V_e means that the fin has more thermal inertia and responds more slowly to changes, so within the fixed observation time period, the temperature field stays closer to its initial state for longer, which increases the averaged efficiency.

4.3 Wave speed analysis

This section investigates how the various parameters affect the propagation speed of the wavefront. Since M^2, R_n, and S_m appear in the source terms and do not affect the wave speed, we restrict attention to the nanofluid parameters (ϕ, shape), V_e, δ^*, and κ. To this end, we examine the temperature profiles at $\tau = 0.5$, shown in Figure 5.

Figure 5 shows that varying the nanofluid parameters (ϕ, shape), V_e, or δ^* shifts the location of the wavefront (i.e., changes the wave speed), whereas varying κ leaves the wave speed unchanged. This behavior follows directly from the structure of the governing equation: expanding the diffusive term in (18) yields

$$\Lambda_D \frac{1}{1+\kappa r}\frac{\partial}{\partial r}\left[(1+\kappa r)(1+\delta^*(\theta-\theta_a))\frac{\partial\theta}{\partial r}\right] = \Lambda_D(1+\delta^*(\theta-\theta_a))\theta_{rr}+\Lambda_D\delta^*\theta_r^2+\Lambda_D\frac{\kappa}{1+\kappa r}(1+\delta^*(\theta-\theta_a))\theta_r.$$

This shows that κ only appears in terms involving the first-order spatial derivative, while it does not contribute to the coefficient of the highest-order term θ_{rr}. Since the equation is second-order hyperbolic in $(\theta_{\tau\tau}, \theta_{rr})$, the local characteristic speed of the equation, evaluated at a point where the solution takes the value θ, is

$$c(\theta) = \sqrt{\frac{\Lambda_D\left[1+\delta^*(\theta-\theta_a)\right]}{V_e^2}}. \tag{38}$$

As confirmed by Figure 5(d), κ affects the amplitude of the temperature behind the wavefront but not its speed, consistent with previous studies showing that the wave speed is independent of the fin profile [45, 46].

The expression (38) also explains the behavior observed in the remaining panels. In Figure 5(a), adding nanoparticles and varying the shape from SS to SC to SP both increase Λ_D, thereby increasing the wave speed and pushing the wavefront to a larger r at the same instant $\tau = 0.5$. Similarly,

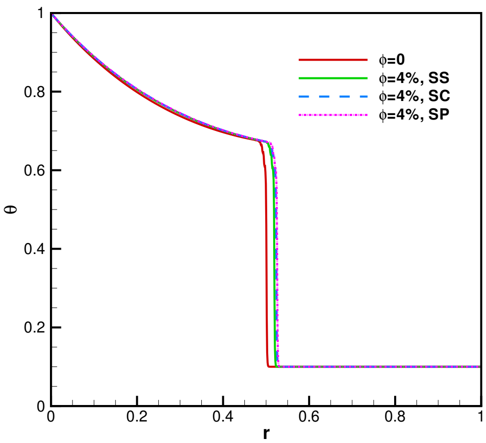

(a) effect of nanofluid

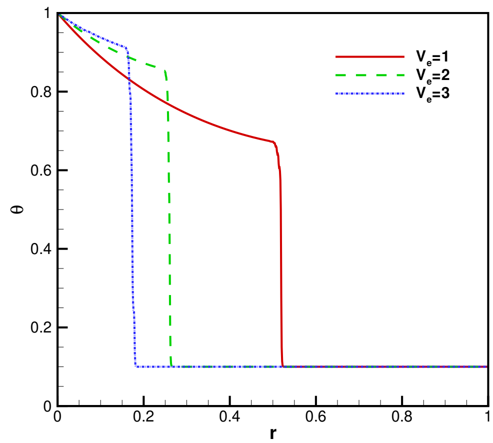

(b) effect of V_e

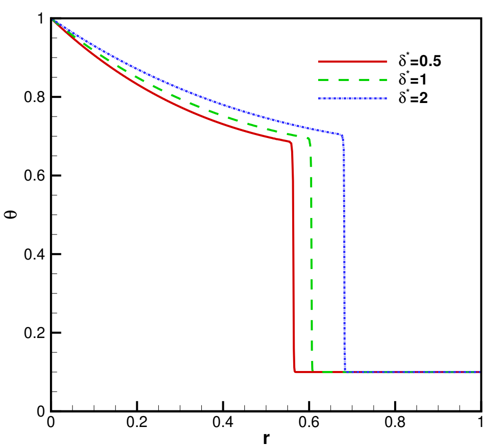

(c) effect of δ^*

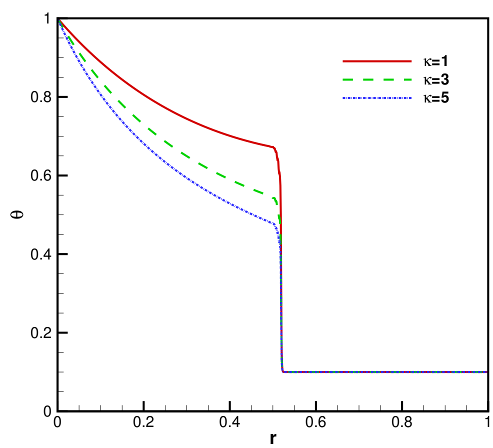

(d) effect of κ

Figure 5: Thermal profiles at $\tau = 0.5$. Common parameters: $\theta_a = 0.1$, $\ell = 1/4$, $M^2 = R_n = S_m = 1$. (a) effect of nanofluid, other parameters: $V_e = 1$, $\kappa = 1$, $\delta^* = 0$; (b) effect of V_e, other parameters: $\kappa = 1$, $\delta^* = 0$, $\phi = 4\%$-SS; (c) effect of δ^*, other parameters: $V_e = 1$, $\kappa = 1$, $\phi = 4\%$-SS; (d) effect of κ, other parameters: $V_e = 1$, $\delta^* = 0$, $\phi = 4\%$-SS.

Figure 5(c) shows that increasing δ^* also increases the wave speed, through the factor $1+\delta^*(\theta-\theta_a)$ in $c(\theta)$. In contrast, increasing V_e slows the wave speed, consistent with the wavefront positions $r \approx 0.52, 0.26, 0.17$ observed in Figure 5(b) for $V_e = 1, 2, 3$, which match the predicted value $r = c\tau = \sqrt{\Lambda_D}\,\tau/V_e$ (since $\delta^* = 0$) almost exactly.

4.4 Long-time thermal performance

While the previous subsection showed that M^2, R_n, and S_m do not affect the propagation speed of the transient wavefront, these parameters can still strongly influence the eventual temperature distribution of the fin. This subsection therefore investigates the effect of these heat-loss mechanisms on the long-time temperature distribution. To this end, we calculate the thermal profile at $\tau = 20$ for each parameter in turn, shown in Figure 6. The figure shows that increasing any of M^2, R_n, or S_m consistently reduces the temperature over the fin, since a larger value corresponds to a stronger heat-loss mechanism, removing more heat from the fin. In addition, increasing κ from 1 to 3 also lowers the temperature at every fixed position r and for every value of M^2, R_n, or S_m, since a larger κ corresponds to a relatively longer fin, whose enlarged lateral area increases the total heat loss. This trend also agrees with that observed in Figure 5(d).

5 Conclusion

This work examined the thermal behavior and heat transfer performance of a wet, porous radial fin saturated with a shape-dependent Al_2O_3–Ag/water hybrid nanofluid, subject to non-Fourier heat conduction and combined convection, radiation, and mass-exchange surface losses. A semi-implicit local discontinuous Galerkin method with a TVB limiter was developed to solve the resulting governing equation, and was employed to assess fin efficiency, transient wavefront propagation, and the long-time thermal response over a wide range of physical and nanofluid parameters. The key findings are summarized as follows.

(i) The addition of hybrid nanoparticles enhances the time-averaged fin efficiency relative to the pure base fluid, with efficiency increasing monotonically with nanoparticle volume fraction.

(ii) Among the three shape combinations examined, the SP combination yields the highest efficiency.

(iii) The efficiency decreases with increasing radius ratio κ, whereas it rises with the thermal lag parameter V_e.

(iv) The wave speed is jointly influenced by the nanoparticle volume fraction and shape, the conductivity coefficient δ^*, and the thermal lag parameter V_e, but is independent of the fin radius ratio κ.

(v) Strengthening any of the convection, radiation, or mass-exchange loss mechanisms reduces the fin temperature in long-time simulations.

References

[1] Z. Yan, C. S. Oon, B. T. Tan, and J. B. Ooi. Geometric design and optimization of extended surfaces for enhanced heat transfer: A comprehensive review. *Results Eng.*, 27:106227, 2025.

[2] M. A. Rahman, S. M. M. Hasnain, P. Paramasivam, and A. G. Ayanie. Advancing thermal management in electronics: a review of innovative heat sink designs and optimization techniques. *RSC Adv.*, 14(43):31291–31319, 2024.

[3] A. Sadeghianjahromi and C.-C. Wang. Heat transfer enhancement in fin-and-tube heat exchangers – A review on different mechanisms. *Renew. Sustain. Energy Rev.*, 137:110470, 2021.

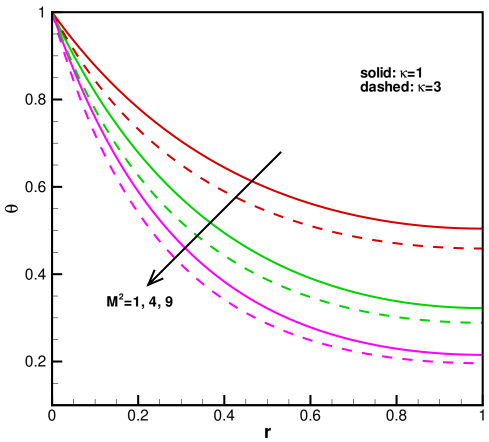

(a) effect of M^2

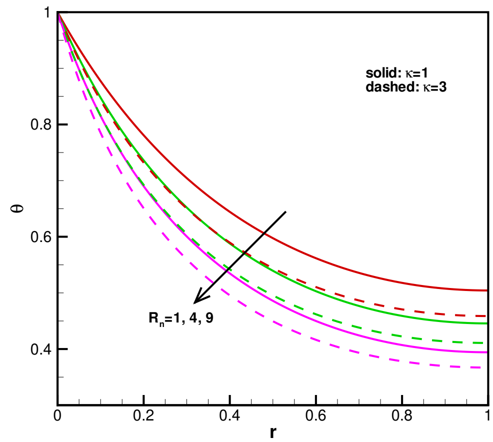

(b) effect of R_n

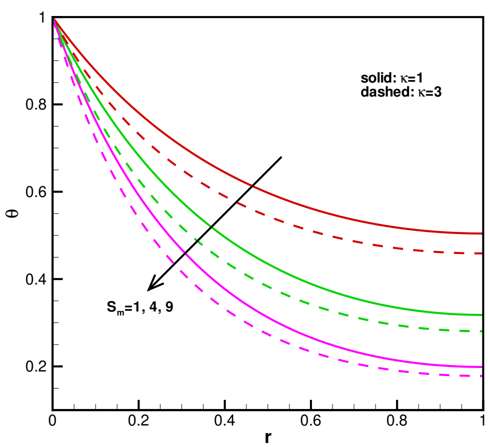

(c) effect of S_m

Figure 6: Effect of parameters M^2, R_n, S_m and κ on the thermal behavior at $\tau = 20$. Common parameters: $V_e = 1$, $\delta^* = 0.1$, $\ell = 1/4$, $\theta_a = 0.1$, $\phi = 4\%$-SS. (a) effect of M^2, $R_n = S_m = 1$; (b) effect of R_n, $M^2 = S_m = 1$; (c) effect of S_m, $M^2 = R_n = 1$.

[4] A. Maji and G. Choubey. Improvement of heat transfer through fins: A brief review of recent developments. *Heat Transf.*, 49(3):1658–1685, 2020.

[5] M. Abbaszadeh and M. Liaghat. Parabolic trough solar collector performance enhancement using bio inspired fins and ternary nanofluids: A combined ANN and CFD energy and exergy analysis. *Renew. Energy*, 268:125833, 2026.

[6] R. S. V. Kumar, R. N. Kumar, G. Sowmya, B. C. Prasannakumara, and I. E. Sarris. Exploration of temperature distribution through a longitudinal rectangular fin with linear and exponential temperature-dependent thermal conductivity using DTM-Pade approximant. *Symmetry*, 14(4), 2022.

[7] I. Ullah, S. Ullah, A. Ali, S. I. Shah, W. Weera, and M. M. Alam. Heat transfer analysis from moving convection-radiative triangular porous fin exposed to heat generation. *Case Stud. Therm. Eng.*, 38:102177, 2022.

[8] S. Riasat, M. Ramzan, C. A. Saleel, M.A. El-Shorbagy, S. Kadry, A. M. Saeed, and S. M. Eldin. A comparative analysis of dovetail and rectangular fins with insulated tips wetted with ZnO-SAE 50 nanolubricant for energy transfer process. *Case Stud. Therm. Eng.*, 51:103576, 2023.

[9] M. Torabi, A. Aziz, and K. Zhang. A comparative study of longitudinal fins of rectangular, trapezoidal and concave parabolic profiles with multiple nonlinearities. *Energy*, 51:243–256, 2013.

[10] S. Hosseinzadeh, K. Hosseinzadeh, A. Hasibi, and D.D. Ganji. Thermal analysis of moving porous fin wetted by hybrid nanofluid with trapezoidal, concave parabolic and convex cross sections. *Case Stud. Therm. Eng.*, 30:101757, 2022.

[11] M. Turkyilmazoglu. Heat transfer from moving exponential fins exposed to heat generation. *Int. J. Heat Mass Transfer*, 116:346–351, 2018.

[12] Z. U. Din, A. Ali, M. De la Sen, and G. Zaman. Entropy generation from convective-radiative moving exponential porous fins with variable thermal conductivity and internal heat generations. *Sci. Rep.*, 12(1):1791, 2022.

[13] M. L. Keerthi, B. J. Gireesha, and G. Sowmya. Numerical investigation of transient thermal behaviour of fully wet and porous moving semi-spherical fin. *Phys. Scr.*, 97(8):085220, 2022.

[14] A. Aziz and F. Khani. Analytic solutions for a rotating radial fin of rectangular and various convex parabolic profiles. *Commun. Nonlinear Sci. Numer. Simul.*, 15(6):1565–1574, 2010.

[15] R. J. Moitsheki. Steady heat transfer through a radial fin with rectangular and hyperbolic profiles. *Nonlinear Anal. Real World Appl.*, 12(2):867–874, 2011.

[16] A. Aziz and M. M. Rahman. Thermal performance of a functionally graded radial fin. *Int. J. Thermophys.*, 30(5):1637–1648, 2009.

[17] R. Jooma and C. Harley. Heat transfer in a porous radial fin: Analysis of numerically obtained solutions. *Adv. Math. Phys.*, 2017(1):1658305, 2017.

[18] T. Patel and R. Meher. A study on convective-radial fins with temperature-dependent thermal conductivity and internal heat generation. *Nonlinear Eng.*, 8(1):145–156, 2019.

[19] Waseem, A. S. Adeyemo, Y. Wang, U. O. Rufai, A. Thaljaoui, and S. M. E. Babiker. Neuro-symbolic modeling of a radiative–convective moving radial fin with temperature-dependent conductivity and heat absorption. *Int. Commun. Heat Mass Transf.*, 175:111218, 2026.

[20] M. Azhdari, G. Rezazadeh, R. Pathak, H.-M. Tautenhahn, F. Tautenhahn, T. Ricken, and S. M. Seyedpour. A critical review of non-Fourier heat transfer theories with phase lag in bio-heating: Explaining the variations in reported phase lag coefficients. *Int. J. Therm. Sci.*, 220(B):110376, 2026.

[21] J. C. Maxwell. On the dynamical theory of gases. *Philos. Trans. R. Soc. Lond.*, 157:49–88, 1867.

[22] C. Cattaneo. Sulla conduzione del calore. *Atti Sem. Mat. Fis. Univ. Modena*, 3:83–101, 1948.

[23] C. Cattaneo. Sur une forme de l'equation de la chaleur eliminant la paradoxe d'une propagation instantantee. *C. R. Acad. Sci.*, 247:431–433, 1958.

[24] J.-Y. Lin. The non-Fourier effect on the fin performance under periodic thermal conditions. *Appl. Math. Modell.*, 22(8):629–640, 1998.

[25] H. Ahmadikia and M. Rismanian. Analytical solution of non-Fourier heat conduction problem on a fin under periodic boundary conditions. *J. Mech. Sci. Technol.*, 25(11):2919–2926, 2011.

[26] S. Singh, D. Kumar, and K. N. Rai. Analytical solution of Fourier and non-Fourier heat transfer in longitudinal fin with internal heat generation and periodic boundary condition. *Int. J. Therm. Sci.*, 125:166–175, 2018.

[27] J. Ma, Y. Sun, and S. Li. Element differential method for non-Fourier heat conduction in the convective-radiative fin with mixed boundary conditions. *Coatings*, 12(12):1862, 2022.

[28] J. Wang, X. Yang, J. J. Klemeš, K. Tian, T. Ma, and B. Sunden. A review on nanofluid stability: preparation and application. *Renew. Sustain. Energy Rev.*, 188:113854, 2023.

[29] H. Yasmin, S. O. Giwa, S. Noor, and M. Sharifpur. Thermal conductivity enhancement of metal oxide nanofluids: A critical review. *Nanomaterials*, 13(3):597, 2023.

[30] M. Sahu and J. Sarkar. Steady-state energetic and exergetic performances of single-phase natural circulation loop with hybrid nanofluids. *J. Heat Transfer*, 141(8):082401, 2019.

[31] M. L. G. Ho, C. S. Oon, L.-L. Tan, Y. Wang, and Y. M. Hung. A review on nanofluids coupled with extended surfaces for heat transfer enhancement. *Results Eng.*, 17:100957, 2023.

[32] G. Sowmya, B. J. Gireesha, and B. C. Prasannakumara. Scrutinization of different shaped nanoparticle of molybdenum disulfide suspended nanofluid flow over a radial porous fin. *Int. J. Numer. Methods Heat Fluid Flow*, 30(7):3685–3699, 2019.

[33] M. Ouada, M. Kezzar, N. Talbi, M. R. Eid, M. R. Sari, W. M. Yousef, and E. M. Elsaid. Heat transfer characteristics of moving longitudinal porous fin wetted with ternary (Cu–Al_2O_3–TiO_2) hybrid nanofluid: ADM solution. *Eur. Phys. J. Plus*, 138(9):861, 2023.

[34] S. Upadhyay, P. Sharma, V. Chaurasiya, and S. S. Rawat. Numerical study of enhanced heat transfer in stretchable/shrinkable fins using nanofluids: a parametric study. *Eur. Phys. J. Plus*, 141(1):50, 2026.

[35] C. G. Pavithra and B. J. Gireesha. Transient thermal analysis in convective–radiative exponential profiled fins in shape-dependent hybrid (MoS_2–TiO_2–$C_6H_{14}O$) nanofluids: a comparative study on Fourier and non-Fourier heat conduction. *J. Therm. Anal. Calorim.*, 150(13):10323–10343, 2025.

[36] C. G. Pavithra, B. J. Gireesha, S. Sushma, and K. J. Gowtham. Analysis of convective-radiative heat transfer in dovetail longitudinal fins with shape-dependent hybrid nanofluids: a study using the Hermite wavelet method. *Appl. Math. Mech.*, 46(2):357–372, 2025.

[37] B. Cockburn and C.-W. Shu. The local discontinuous Galerkin method for time-dependent convection-diffusion systems. *SIAM J. Numer. Anal.*, 35(6):2440–2463, 1998.

[38] B. Cockburn and C.-W. Shu. TVB Runge-Kutta local projection discontinuous Galerkin finite-element method for conservation-laws .II. general framework. *Math. Comput.*, 52(186):411–435, 1989.

[39] M. L. Keerthi, B. J. Gireesha, and G. Sowmya. Numerical investigation of efficiency of fully wet porous convective-radiative moving radial fin in the presence of shape-dependent hybrid nanofluid. *Int. Commun. Heat Mass Transf.*, 138:106341, 2022.

[40] R. R. Sahoo. Thermo-hydraulic characteristics of radiator with various shape nanoparticle-based ternary hybrid nanofluid. *Powder Technol.*, 370:19–28, 2020.

[41] P. L. Ndlovu and R. J. Moitsheki. Analysis of temperature distribution in radial moving fins with temperature dependent thermal conductivity and heat transfer coefficient. *Int. J. Therm. Sci.*, 145:106015, 2019.

[42] R. M. S. da Gama. Simulation of the steady-state energy transfer in rigid bodies, with convective/radiative boundary conditions, employing a minimum principle. *J. Comput. Phys.*, 99(2):310–320, 1992.

[43] S. Mosayebidorcheh, M. Hatami, T. Mosayebidorcheh, and D. D. Ganji. Optimization analysis of convective–radiative longitudinal fins with temperature-dependent properties and different section shapes and materials. *Energy Convers. Manage.*, 106:1286–1294, 2015.

[44] Y. Xu and C.-W. Shu. Local discontinuous Galerkin methods for high-order time-dependent partial differential equations. *Comm. Comput. Phys.*, 7(1):1–46, 2010.

[45] K. Bamdad, A. Azimi, and H. Ahmadikia. Thermal performance analysis of arbitrary-profile fins with non-Fourier heat conduction behavior. *J. Eng. Math.*, 76(1):181–193, 2012.

[46] W. Wu and C.-W. Shu. Numerical simulations of non-Fourier heat transfer in longitudinal fin using local discontinuous Galerkin methods. *Appl. Therm. Eng.*, 293:130547, 2026.

Appendix A

First, let $\theta_s(r)$ solve the steady-state problem

$$\theta_s'' = M^2(\theta_s - \theta_a), \qquad \theta_s(0) = 1, \quad \theta_s'(1) = 0, \tag{A1}$$

which gives

$$\theta_s(r) = \theta_a + (1 - \theta_a)\, \frac{\cosh[M(1-r)]}{\cosh M}. \tag{A2}$$

Next, setting $u(r,\tau) = \theta(r,\tau) - \theta_s(r)$ isolates the homogeneous transient part, which satisfies

$$u_{\tau\tau} + u_\tau + M^2 u = u_{rr}, \qquad u(0,\tau) = 0, \quad u_r(1,\tau) = 0, \tag{A3}$$

$$u(r,0) = \theta_a - \theta_s(r), \qquad u_\tau(r,0) = 0. \tag{A4}$$

Separating variables $u = R(r)T(\tau)$ in (A3) gives the spatial eigenproblem

$$R'' + \lambda^2 R = 0, \qquad R(0) = 0, \quad R'(1) = 0, \tag{A5}$$

with eigenpairs

$$R_n(r) = \sin(\lambda_n r), \qquad \lambda_n = \frac{(2n-1)\pi}{2}, \quad n = 1, 2, 3, \ldots, \tag{A6}$$

which are orthogonal on $[0,1]$ with $\int_0^1 \sin^2(\lambda_n r)\, dr = \frac{1}{2}$. The corresponding temporal equation is

$$T_n'' + T_n' + (M^2 + \lambda_n^2)T_n = 0, \tag{A7}$$

whose solution is

$$T_n(\tau) = e^{-\tau/2}\big[a_n \cos(\mu_n \tau) + b_n \sin(\mu_n \tau)\big], \qquad \mu_n = \sqrt{M^2 + \lambda_n^2 - \tfrac{1}{4}}. \tag{A8}$$

Expanding the initial data (A4) in the eigenbasis (A6) and using $u_\tau(r,0) = 0$ then yields

$$a_n = -\frac{2(1-\theta_a)\lambda_n}{M^2 + \lambda_n^2}, \qquad b_n = \frac{a_n}{2\mu_n}. \tag{A9}$$

Finally, combining (A2), (A6), (A8), and (A9) leads to (32).